Supplement of Atmos. Meas. Tech., 15, 3747–3760, 2022
https://doi.org/10.5194/amt-15-3747-2022-supplement

Atmospheric Measurement Techniques
Open Access
EGU

Supplement of

High-frequency gaseous and particulate chemical characterization using extractive electrospray ionization mass spectrometry (Dual-Phase-EESI-TOF)

Chuan Ping Lee et al.

Correspondence to: Imad El Haddad (imad.el-haddad@psi.ch), Dongyu Wang (dongyu.wang@psi.ch), Houssni Lamkaddam (houssni.lamkaddam@psi.ch), and Jay G. Slowik (jay.slowik@psi.ch)

Section S1. Materials

Acetonitrile (Sigma-Aldrich, UV grade), sodium iodide (Sigma-Aldrich, 99.7% purity) and milli-Q water were used to prepare the electrospray (ES) solution. Polyimide-coated fused silica capillary (i.d. 75 μm, o.d. 369 μm; BGB Analytik, Boeckten, Switzerland), HEPA capsule filter (Pall Corporation), and charcoal denuders (Ionicon GmbH, Austria) were used for the electrospray ionization inlet. Ethyl acetate (Sigma-Aldrich, 98% purity), ethyl propionate (Sigma-Aldrich, 98% purity), 3-pentanone (Sigma-Aldrich, 98% purity), camphor (Sigma-Aldrich, 98% purity), hydroxyacetone (Sigma-Aldrich, 98% purity), cis-pinonic acid (Sigma-Aldrich, 98% purity), sebacic acid (Sigma-Aldrich, 98% purity), levoglucosan (Sigma-Aldrich, 98% purity), iodic acid (Sigma-Aldrich, 98% purity), sucrose (Sigma-Aldrich, 98% purity), ammonium nitrate (Sigma-Aldrich, 98% purity), ammonium sulfate (Sigma-Aldrich, 98% purity) were used as the chemical standards for the calibration and SOA formation experiments.

Section S2. Dual-EESI Inlet Sampling Performance

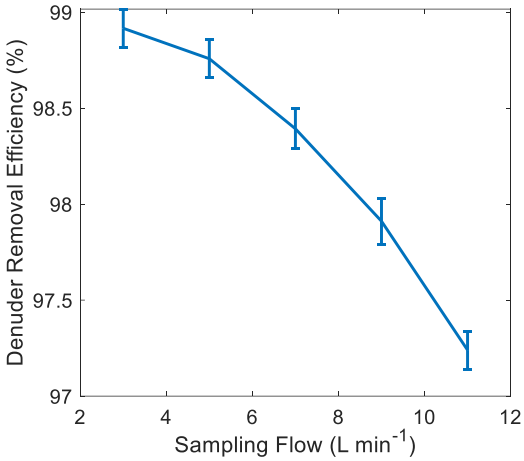

Figure S1. Dual-EESI denuder removal efficiency for camphor gas with a concentration of 100 ppbv at different sampling flows.

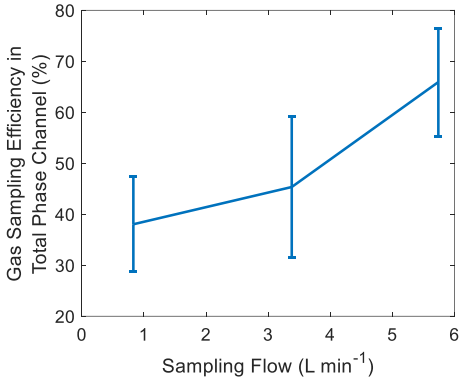

Figure S2. Measurement of semivolatile ($C_9H_{12}O_4$) sampling efficiency in Dual-EESI total-phase (TP) channel (L: 700 mm, OD: 10 mm and ID: 8 mm) at different sampling flows using an acetate-CIMS. The $C_9H_{12}O_4$ was generated by OH· oxidation of 1,2,4-trimethylbenzene at 30% RH and room temperature. The gas sampling efficiency is defined as the ratio between the $C_9H_{12}O_4$ concentration after and before the Dual-EESI total-phase (TP) channel.

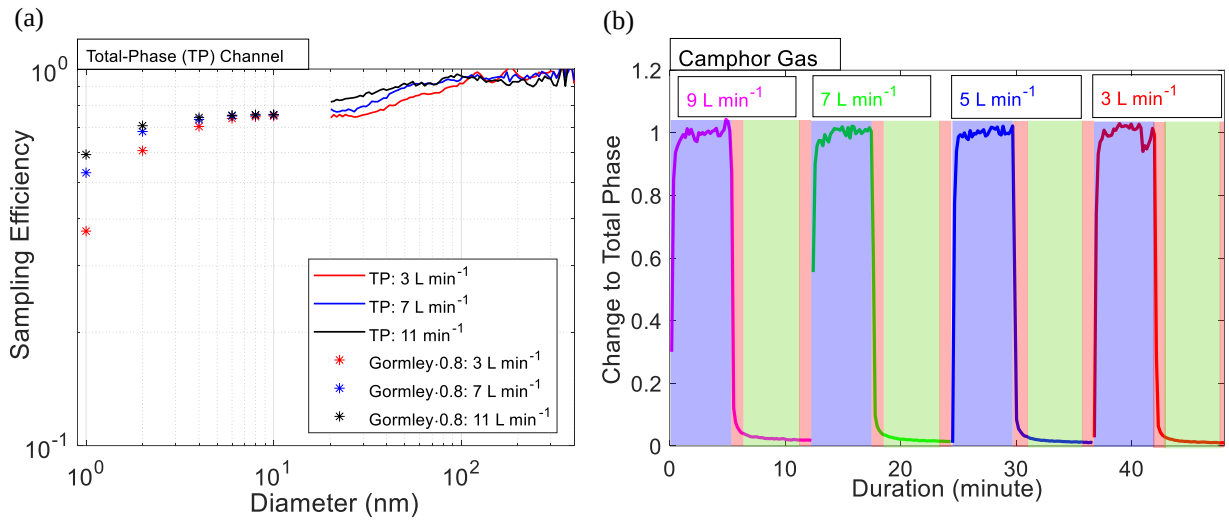

Figure S3. (a) Sampling efficiency of particles at different sampling flows in TP channel of Dual-EESI measured by an SMPS. We used a theoretical calculation (based on Gormley et al. (1949)) to fit the measured particle sampling efficiency of TP for particle size ranges between 1-20 nm (Gormley and Kennedy, 1949). (b) Camphor measurement of Dual-EESI at different sampling flows (3 - 9 L min^{-1}) as colored. The sampling sequences were indicated by the color shades with 5 minutes of total-phase (TP) measurement (blue shade), 1 minute of particle-filter phase (FP) measurement (red shade), 5 minutes of particle-phase (PP) measurement (green shade), and 1 minute of FP (red shade) cycle.

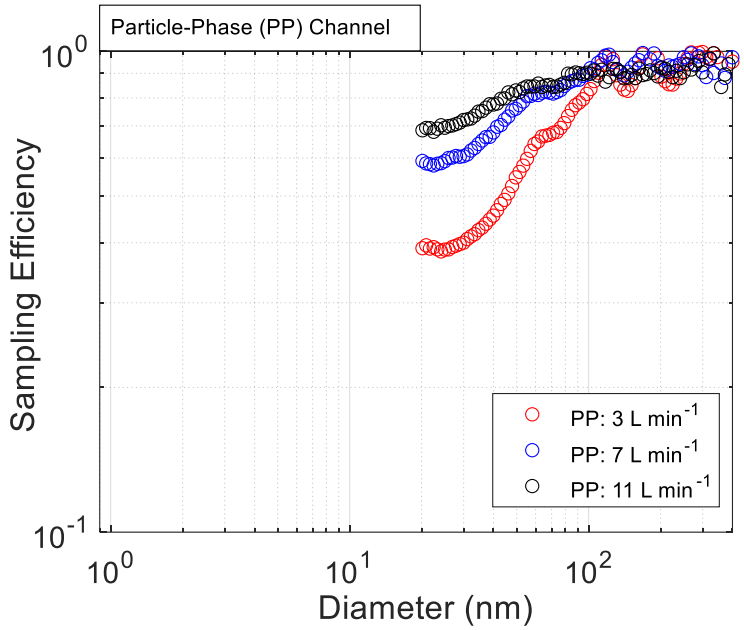

Figure S4. Sampling efficiency of particles at different sampling flows in PP channel of the Dual-EESI measured by an SMPS.

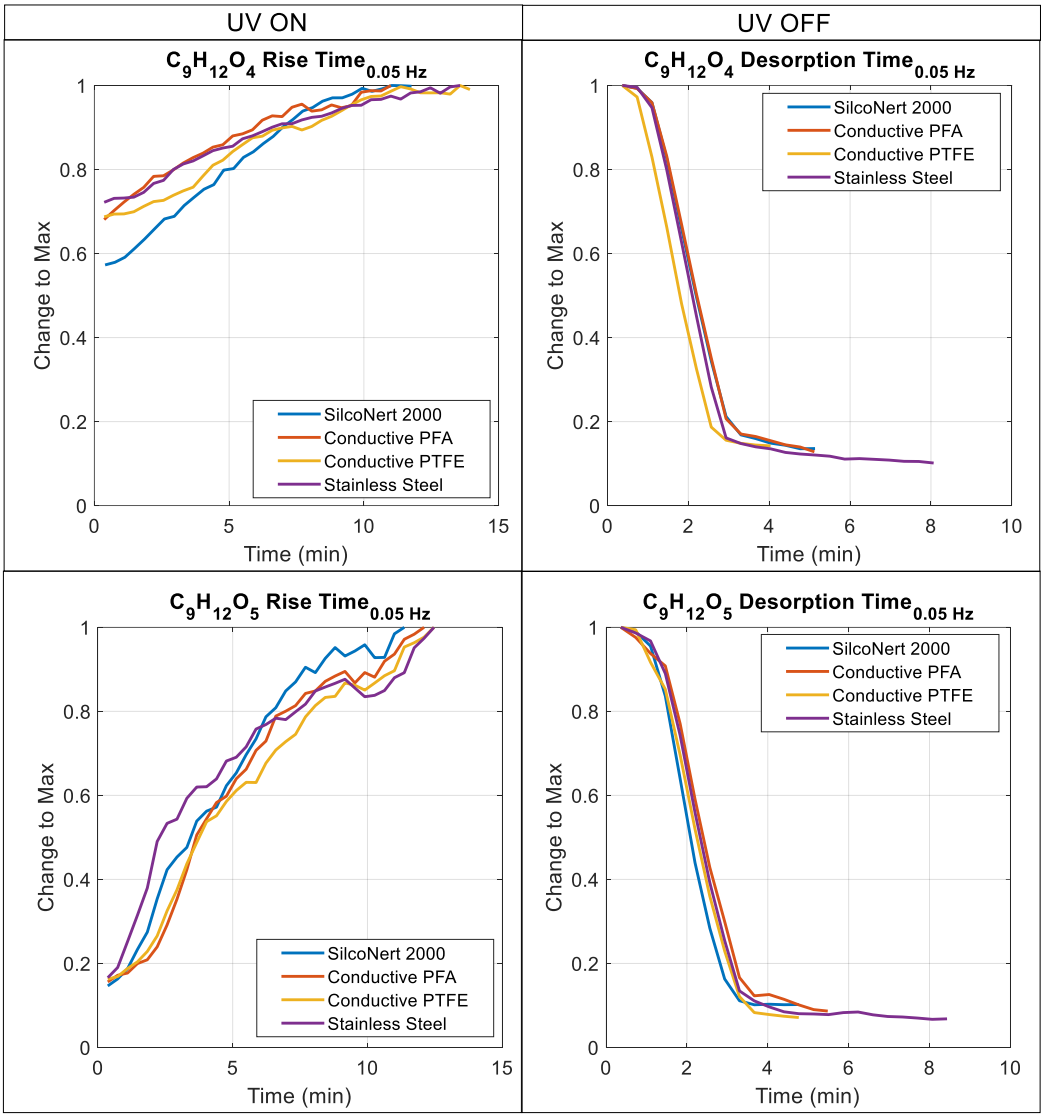

Figure S5. Measurement response changes of $C_9H_{12}O_{4\text{-}5}$ ($\log(c^*)$ = 0.06 and -1.97 µg m^{-3}, respectively, calculated using molecular formula according to (Donahue et al, 2011)) when UV lamp was turned on/off for OH· oxidation of 1,2,4-trimethylbenzene at 30% RH and room temperature for different Dual-EESI inlet tubing materials. The measurements were acquired with 1 Hz measurement resolution and post-averaged by 20 seconds as presented here. The oxidation product signal was measured by an Eisele-type atmospheric pressure chemical ionization inlet (Nitrate-CIMS) connected after the Dual-EESI inlet at 10 L min^{-1} sampling flow. SilcoNert 2000 is stainless-steel tube coated with functionalized hydrogenated amorphous silicon (SilcoNert Inert Coating, Silcotek GmbH).

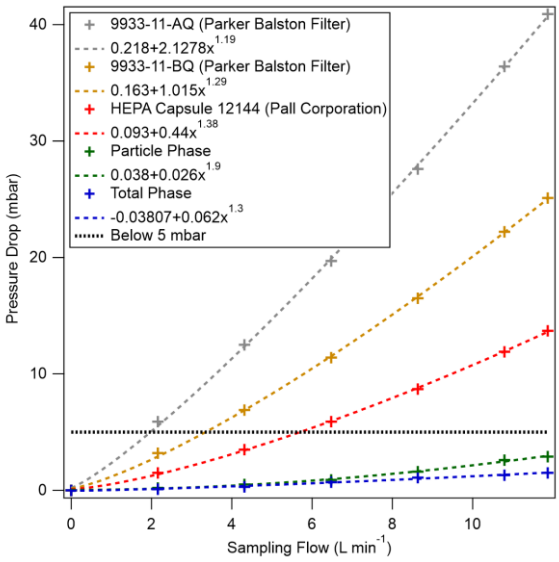

Figure S6. Pressure drops in different sampling channels of the Dual-EESI where three different types of particle filters were characterized in the particle filter channel.

Section S3. Experimental setups

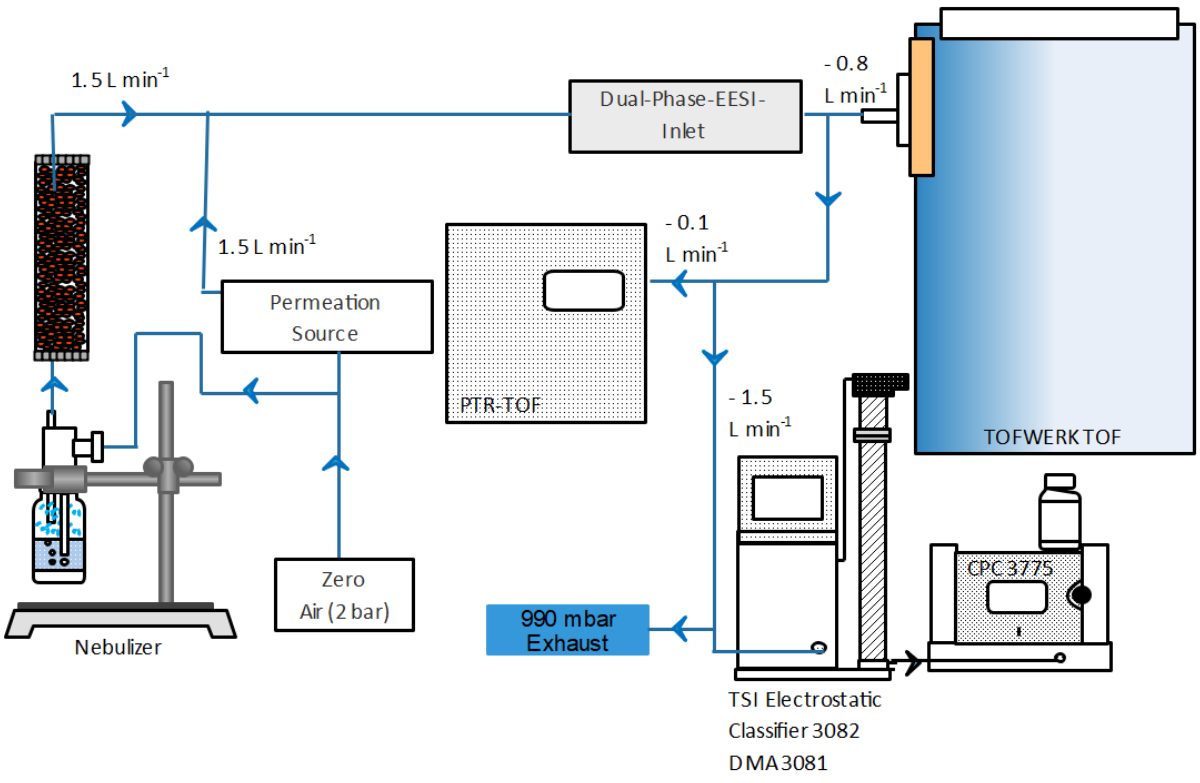

Figure S7. Experimental setup for proof-of-principle measurements of the Dual-EESI using different sampling sequences. Camphor gas from a permeation source was mixed into a stream of levoglucosan particles generated by a nebulizer.

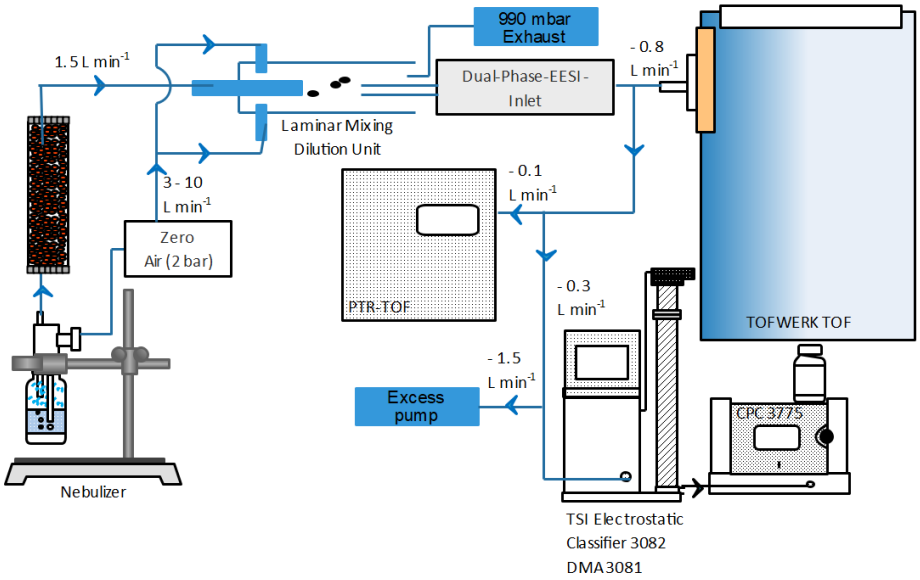

Figure S8. Experimental setup for particle-phase calibration of the Dual-EESI.

(a) (b)

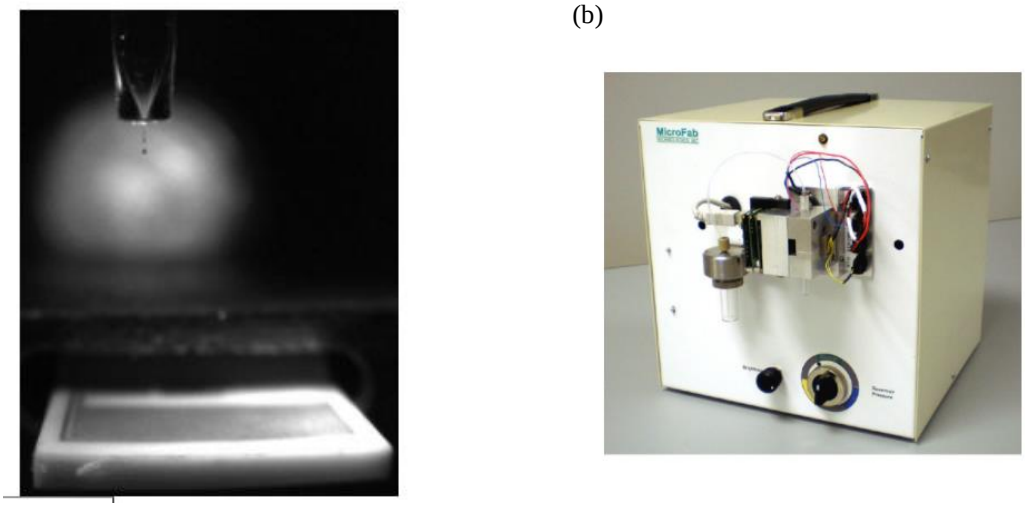

Figure S9. Vaporjet from MicroFab Technologies. (a) View of the microjet dispenser where the droplets are dispensed and evaporated by the white heater. (b) The whole instrument is equipped with different pressure regulators and a stroboscopic camera (VaporJet, MicroFabTechnologies).

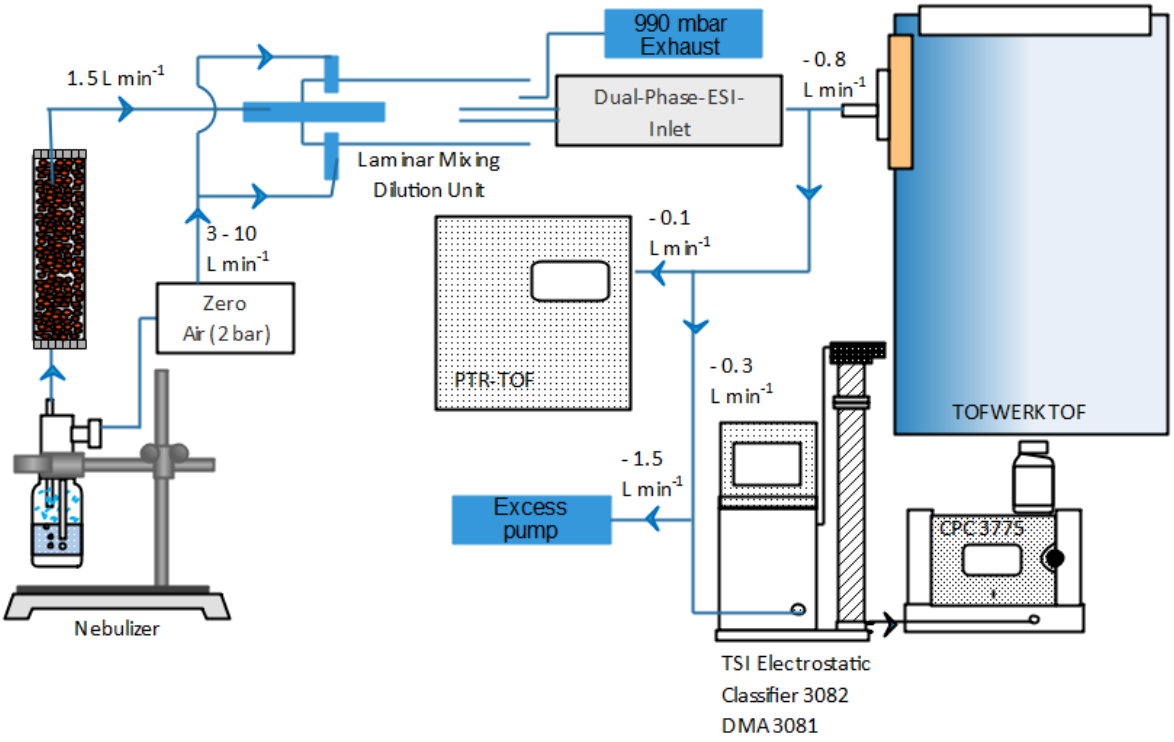

Figure S10. Experimental setup for the Dual-EESI matrix effect measurements by testing a decreasing camphor gas concentration at a constant iodic acid and levoglucosan particle injections.

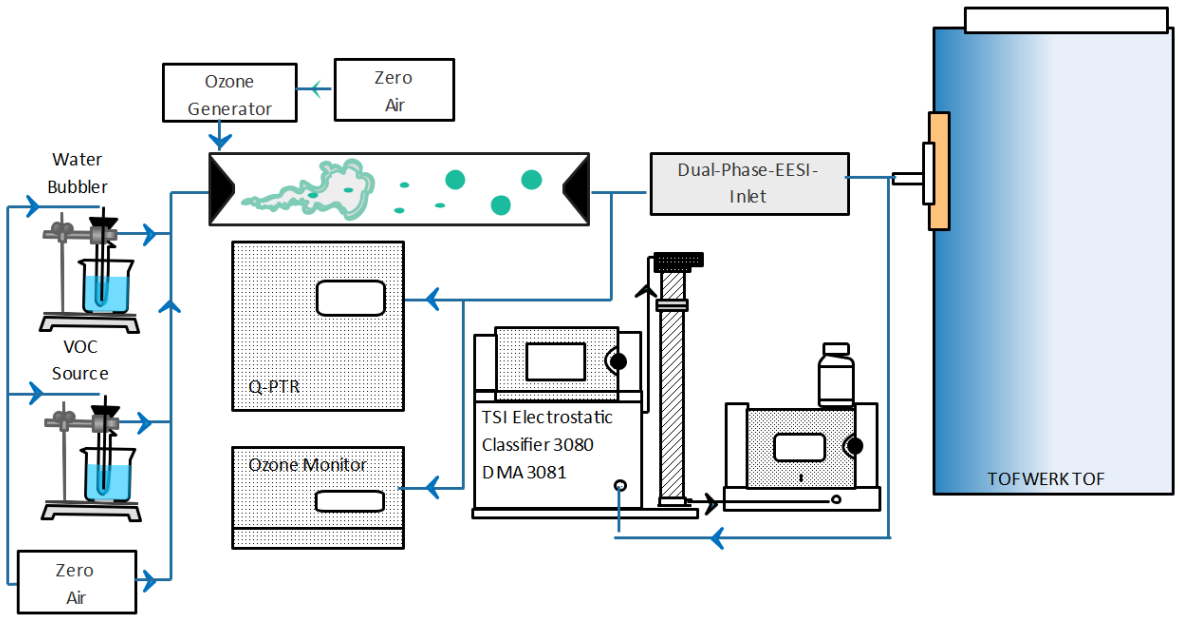

Figure S11. Schematic of the experimental setup for α-pinene new particle formation in a flow tube reactor.

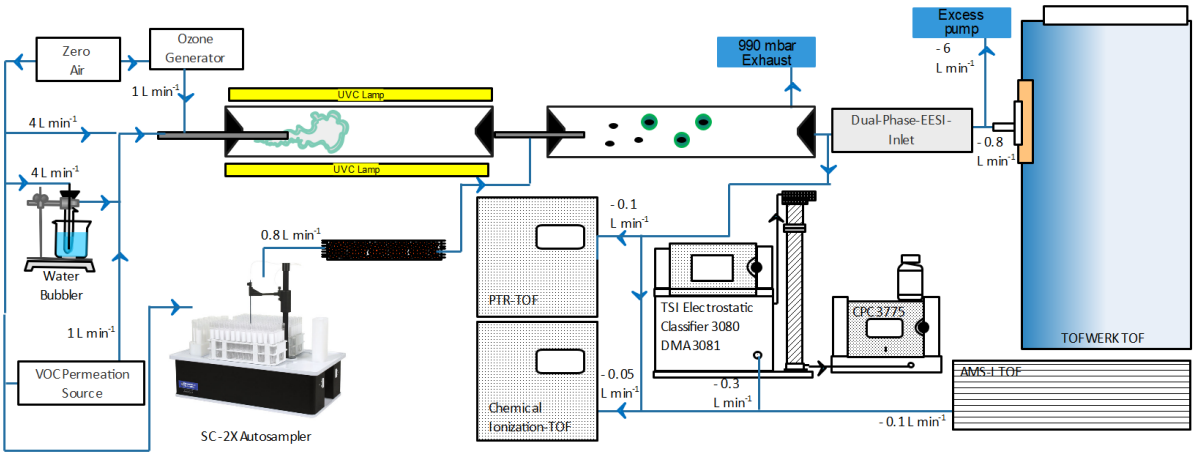

Figure S12. Schematic of the experimental setup for coating experiments. 1,3,5-trimethylbenzene was oxidized in the first flow tube that is surrounded by UV-B lamps. Inorganic particles ($(NH_4)_2SO_4$) are injected into the second flow tube that act as condensation sinks for the low volatility gases that were produced from the first flow tube.

Table S1. Ammonium sulfate nebulization solution concentration with the calculated condensation sink by using the number size distribution of the particle as measured by an SMPS. The condensation sinks were calculated according to the several works mentioned here (Krechmer et al., 2017; Kulmala and Wagner 2001).

Index no.	Nebulization Solution Molarity (mol L^{-1})	Volumetric Geometric Mean Diameter (nm)	Mass concentration (µg m^{-3})	Calculated Condensation Sink (s^{-1})
1	0.25	91.4	680	0.0770
2	0.5	105.5	1125	0.1075
3	0.75	109.4	1319	0.1185
4	1	121.9	1459	0.1291
5	1.5	126.3	1855	0.1574

Section S4. Dual-EESI Characterization

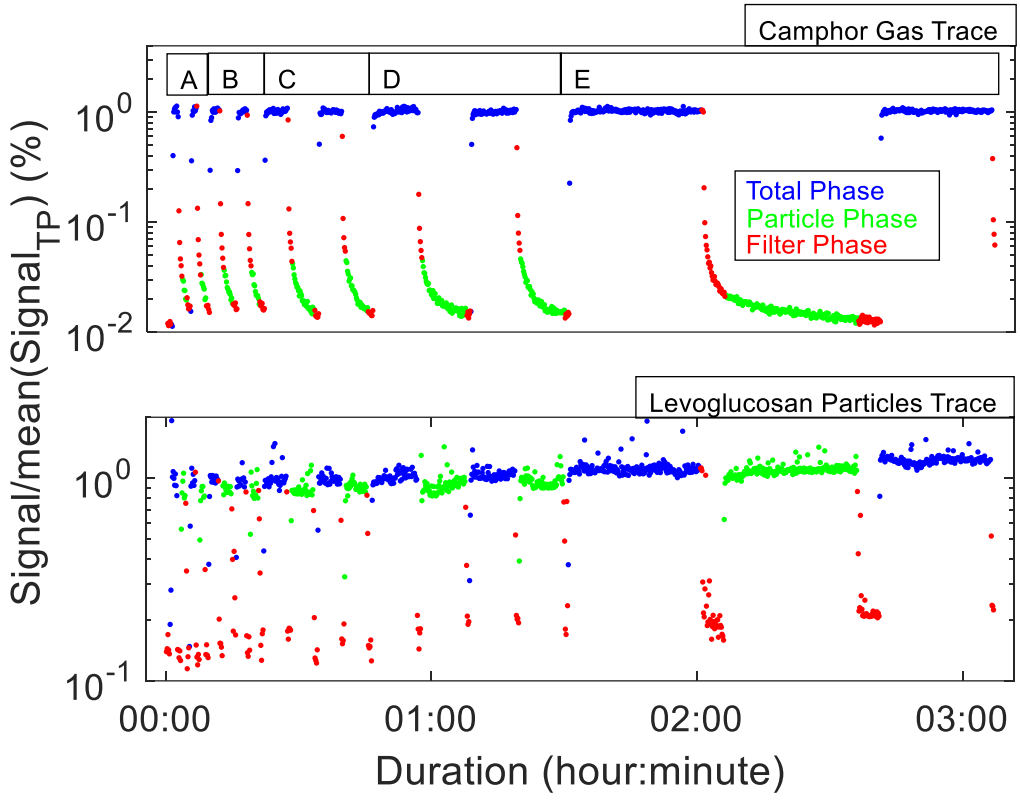

Figure S13. Dual-EESI measurements of levoglucosan and camphor after 10 seconds of pre-averaging. Different ratios of background-to-sampling measurement periods (A, B, C, D and E as tabulated in Table S2) were tested for total-phase (blue marker), particle-phase (green marker) and particle filter (red marker) channel measurements.

Table S2. Sampling periodicity for different sampling sequence type between total-phase, particle-phase and particle filter channels.

Sequence Type	**Total-Phase Channel (minute)**	**Particle-Phase Channel (minute)**	**Particle Filter Channel, Background (minute)**	**Background/ Sampling Measurement Period Ratio**
A	1	1	1	1
B	2	2	1	0.5
C	5	5	1	0.2
D	10	10	1	0.1
E	30	30	5	0.17

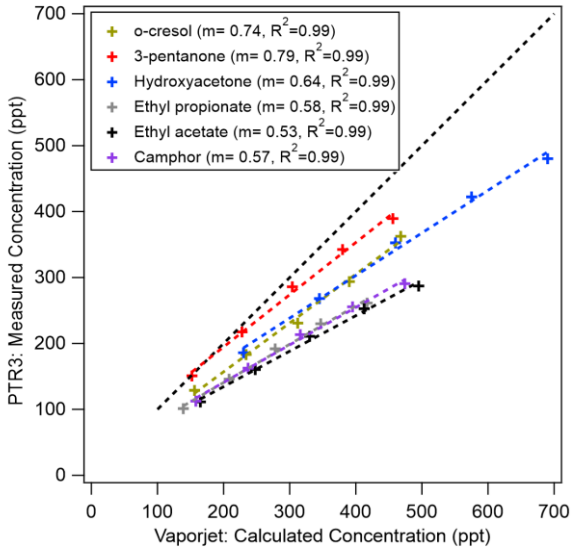

Figure S14. Performance of Vaporjet for vaporizing semi-volatile species in aqueous droplets as a gas generation system to calibrate the Dual-EESI. The performance was demonstrated by the comparison of the measured concentration from proton-transfer-reactor mass spectrometer to the theoretically calculated concentration by assuming that the generated droplets are spherical and fully evaporated on the white heater of the Vaporjet (see Figure S9).

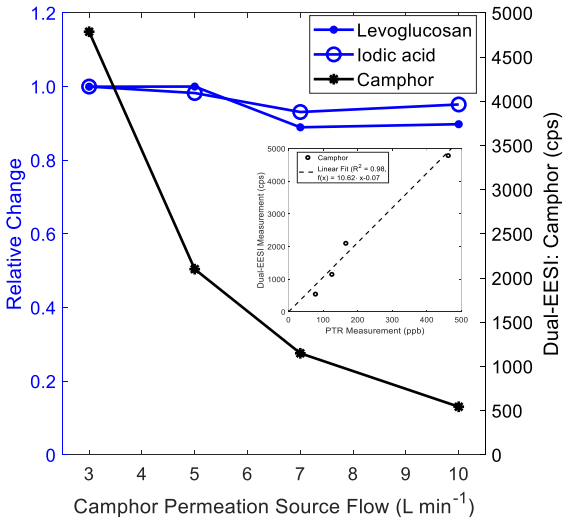

Figure S15. Matrix effect measurement of decreasing gas concentration at constant particle concentration of the Dual-EESI. (Left axis) Relative change of measured intensity from constant nebulization of 0.5 ppm levoglucosan and 0.5 ppm of iodic acid solution with (Right axis) increasing injection flow of camphor permeation source at constant permeation rate. Inset figure shows the camphor measurement comparison between the Dual-EESI (TP measurement) and PTR-TOF.

Section S5. SOA formation additional figures

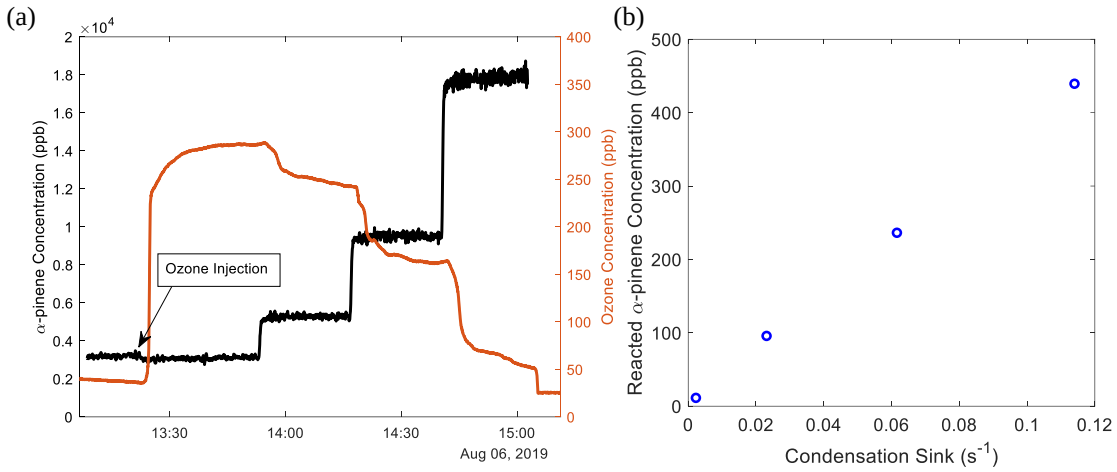

Figure S16. α-pinene SOA formation experiment. (a) Measurement of α-pinene concentration by Q-PTR and ozone concentration by an ozone analyzer. (b) Reacted α-pinene concentration is estimated by multiplying 1.8 on the reacted ozone concentration as the function of condensation sink calculated from the particle number size distribution using an SMPS (Zhang and Zhang, 2005).

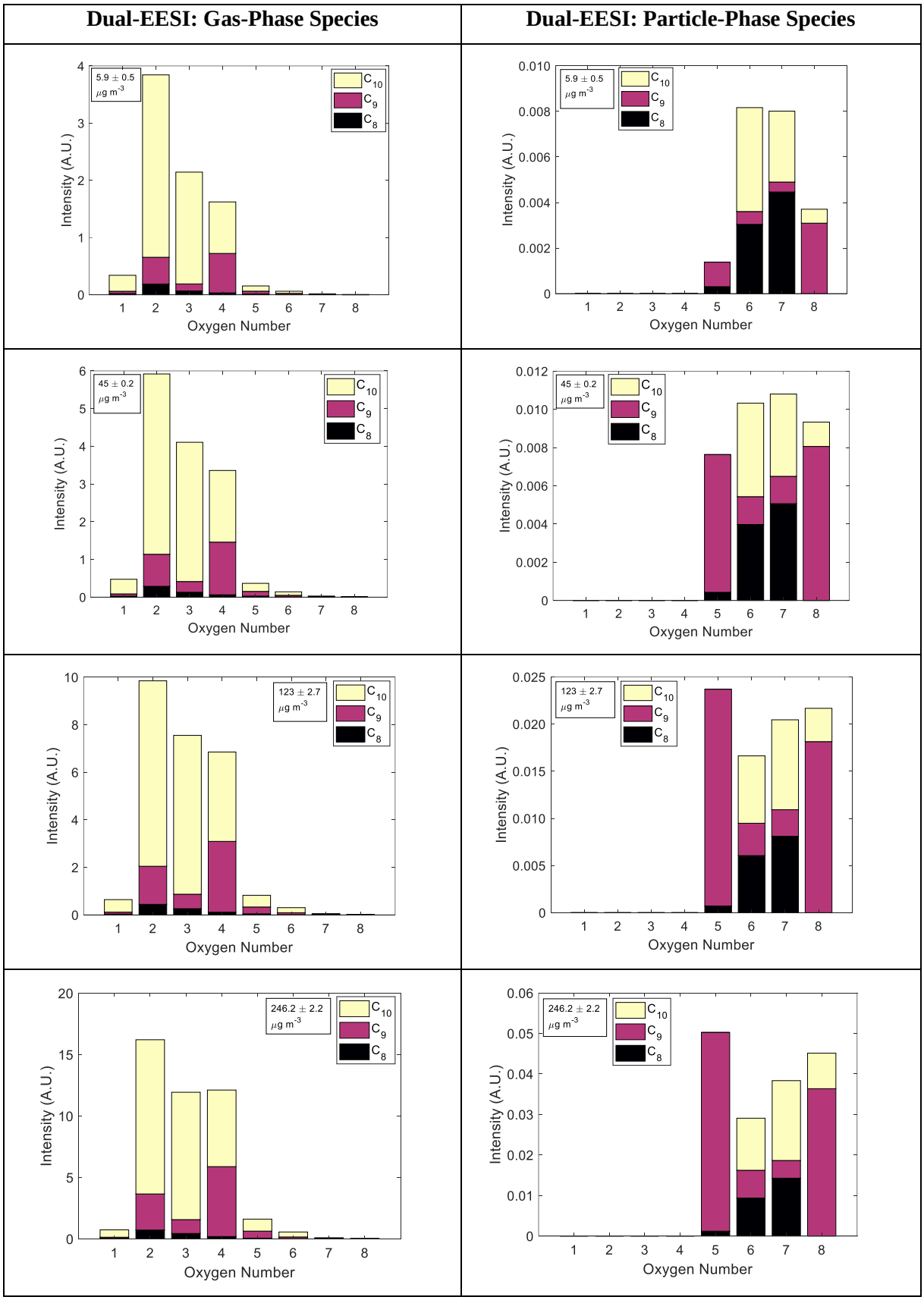

Figure S17. Comparison of (left figures) gas- and (right figures) particle-phase measurements of Dual-EESI for AP SOA mass concentration ranging from 6 – 247 μg m^{-3}.

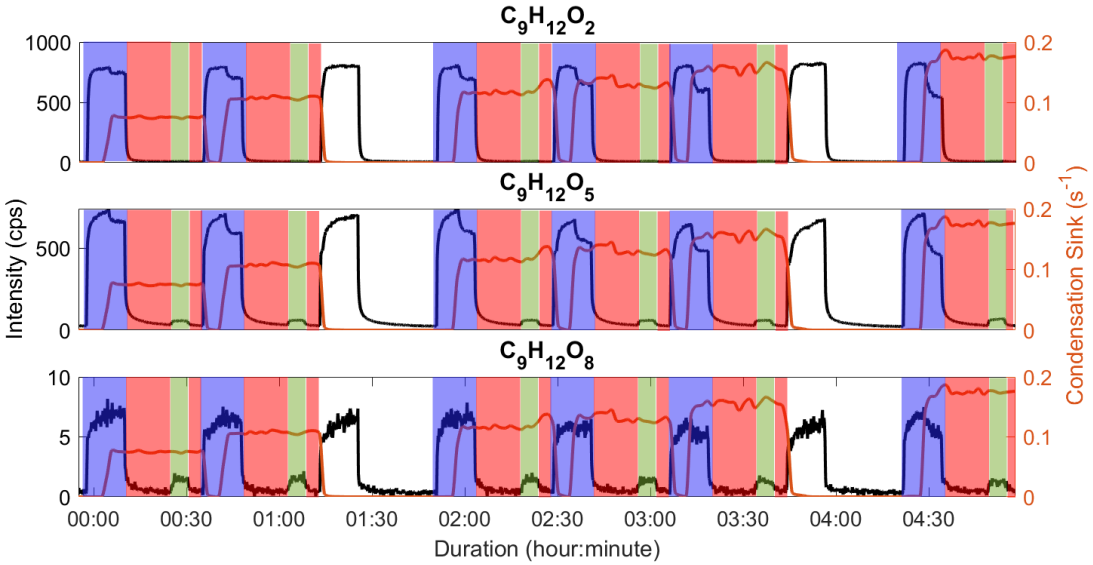

Figure S18. Dual-EESI measurements at different condensation sinks for TMB oxidation products. The condensation sink was increased due to the increasing concentration of injected ammonium sulfate particles (see Table S1). The sampling sequence is indicated by the color shade as (blue shade) TP, (green shade) PP and red shade (FP). The white shades (2 stages) denote the condensation sink stages where no condensation seeds (ammonium sulfate particles) were injected as blank measurements to show that there is no measurable condensation of TMB oxidation products.

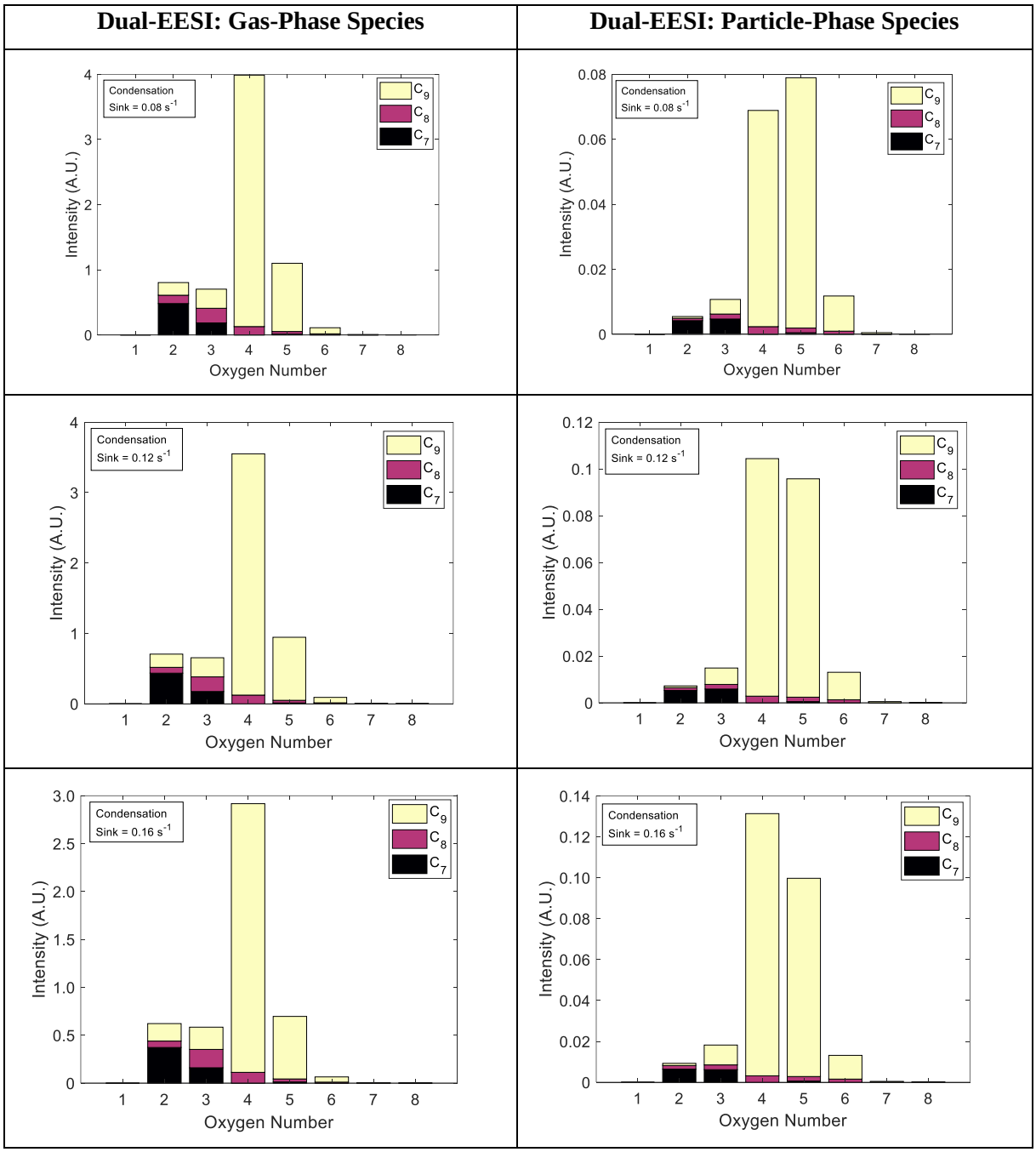

Figure S19. Comparison of (left figures) gas- and (right figures) particle-phase measurements of Dual-EESI for TMB SOA at constant oxidized gas species production rate with increasing condensation sink from 0.08 to 0.16 s^{-1}.

	SOA formation of AP with increasing oxidized gas-phase production rate.	**SOA formation of TMB at constant oxidized gas-phase production rate with increasing condensation sink.**
Gas-phase Chg. to Max.	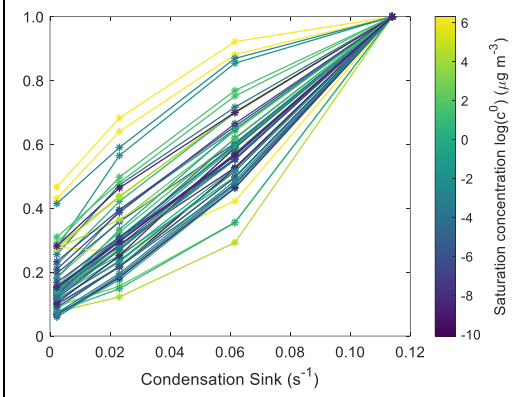	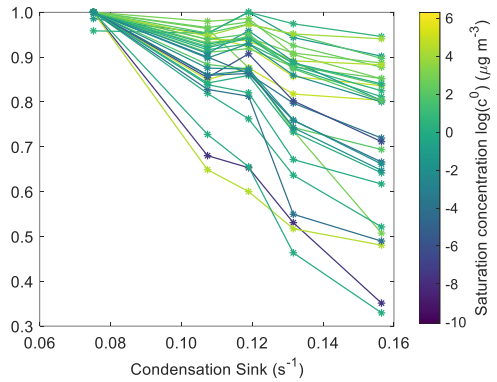
Condensed Phase Chg. to Max.	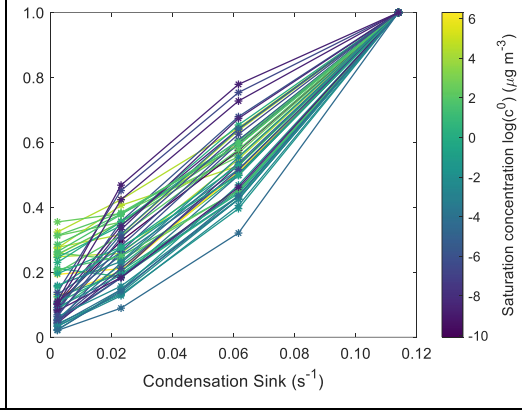	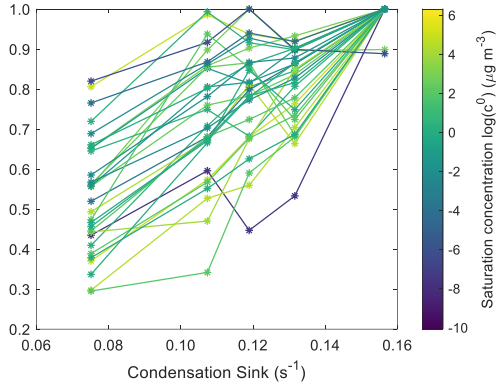

Figure S20. Comparison of the relative changes in the gas- and particle-phase measurements using the Dual-EESI after subtraction and normalization by their respective maxima. All data points were color-scaled by the saturation concentration estimated by Donahue et al. (2011). (Left-panel) SOA formation using α-pinene as precursor and ozone as oxidant, the condensation sink increased due to the increased formation rate of SOA from increasing production rate of oxidation products ($C_{8\text{-}10}H_{12\text{-}16}O_{1\text{-}8}$). (Right-panel) SOA formation using 1,2,4-trimethylbenzene as a precursor and OH as oxidant. The SOA formation rate was increased due to increased injection of condensation sinks at a constant production rate of the oxidation products ($C_{7\text{-}9}H_{8\text{-}16}O_{1\text{-}7}$). Note that similar molecules (See Table Table S3) were chosen purpose for this comparison using the same saturation concentration estimation parameterization. The condensation sinks were calculated as in the reported works (Krechmer et al., 2017; Kulmala and Wagner, 2001).

Table S3. Molecules that are included for AP and TMB SOA.

AP SOA		TMB SOA	
$C_8H_{12}O_{1\text{-}7}$	$C_9H_{14}O_{3\text{-}8}$	$C_7H_8O_{2\text{-}3}$	$C_9H_{12}O_{2\text{-}5,7}$
$C_8H_{13}O_{1\text{-}2}$	$C_9H_{16}O_{3\text{-}8}$	$C_7H_{10}O_{2,3,5,8}$	$C_9H_{13}O_{3\text{-}4}$
$C_8H_{14}O_{1\text{-}5,9}$	$C_{10}H_{12}O_{3\text{-}8}$	$C_8H_{10}O_{2\text{-}4}$	$C_9H_{14}O_{3\text{-}6}$
$C_8H_{16}O_{2\text{-}5}$	$C_{10}H_{14}O_{3\text{-}8}$	$C_8H_{12}O_{2\text{-}5}$	$C_9H_{15}O_{4,6}$
$C_9H_{12}O_{3\text{-}8}$	$C_{10}H_{16}O_{3\text{-}8}$	$C_8H_{14}O_{4,6}$	$C_9H_{16}O_{4\text{-}5}$
		$C_9H_8O_3$	

Section S6. Gas- and particle-phase sensitivity calculation

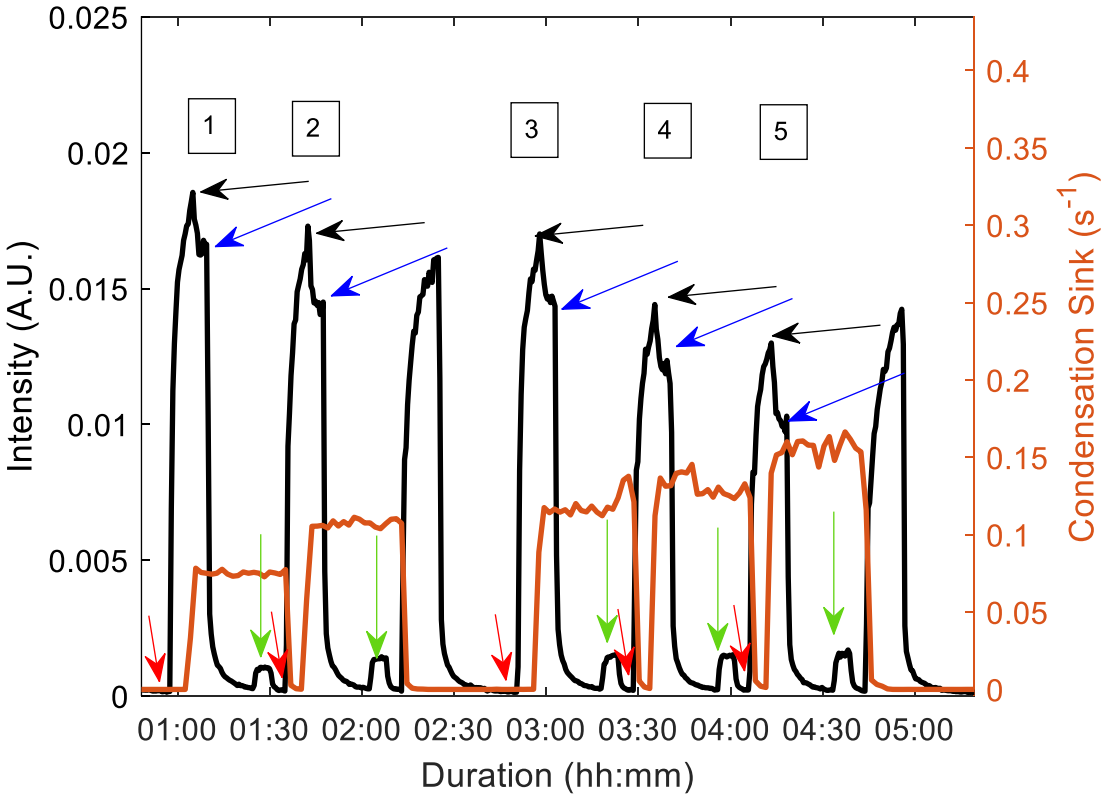

Figure S21. Dual-EESI measurements of gas- and particle-phase of $C_9H_{14}O_5$ at different condensation sinks under a constant TMB oxidation rate for calibration of gas/particle sensitivity response of the Dual-EESI. There are 7 stages of condensation sinks shown above where no ammonium sulfate seeds were injected for these two stages (01:14 - 01:55 and 03:45 - 04:18). These two stages were used to make sure that the background measurements remain the same, showing no TMB SOA is produced when the seeds are not injected.

5 different seed concentrations with condensation sink (Table S1) of 0.08, 0.11, 0.12, 0.13, 0.15 s^{-1} and volumetric geometric mean diameter of 91.4, 105.5, 109.4, 121.9, 126.6 nm were selected for the calibration of the gas/particle sensitivity response measurements. These 5 chosen condensation sinks were chosen because they have the least size-dependent sensitivity due to the nature of coagulation between ES droplet and the particle where the particles within this size range are fully extracted as reported in the work here (Lee et al., 2021).

The drop in measured gas-phase intensity due to injection of condensation seeds, ΔG is defined as

$$G_{without\ CS} = \text{black arrow - red arrow}$$

$$G_{remaining\ with\ CS} = \text{blue arrow - green arrow}$$

$$\Delta G = G_{\text{without CS}} - G_{\text{remaining with CS}} \quad \text{Eq. S1}$$

as denoted in Figure S21. The increase in particle-phase intensity due to injection of condensation seeds, ΔP is defined as

$$\Delta G = \text{green arrow - red arrow,} \quad \text{Eq. S2}$$

where ΔP was corrected according to Eq. S3. Then, the $\Delta G/\Delta P$ sensitivity response is calculated by averaging five CS conditions of $\Delta G/\Delta P$ in Figure S21 for a list of 62 molecules (Table S4). Please see Figure S23 for the performance of the averaging.

Dual-EESI particle-phase measurement correction

Particle-phase intensity is affected by the particle size-dependent sensitivity and the particle transmission efficiency. Thus the corrected particle-phase intensity is defined as

$$\boldsymbol{P_{corrected}} = \frac{\boldsymbol{PP-FP}}{\boldsymbol{S(D_P)\zeta(D_P)}}, \quad \text{Eq. S3}$$

where PP is the measured intensity in particle-phase channel and FP is the measured intensity in particle filter channel. The $S(D_P)$ is the particle size-dependent sensitivity (Lee et al., 2021) parameterized as $34.18D_p^{-0.8692}+0.393$ using AP SOA with particle diameter D_p, as shown in Figure S22. The $\zeta(D_P)$ is the empirically measured particle sampling efficiency of the Dual-EESI inlet as shown in Figure S4.

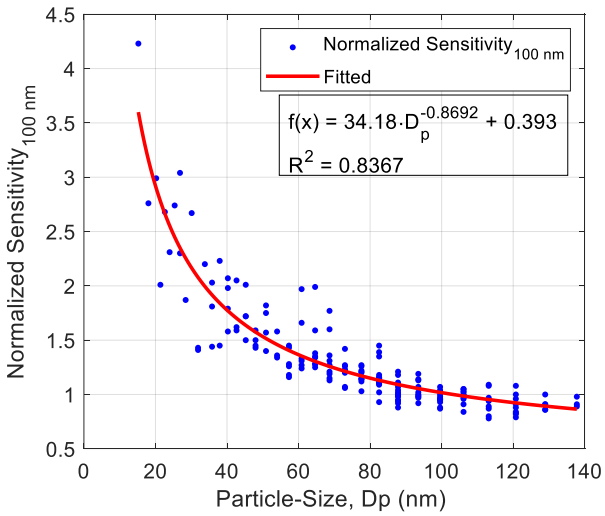

Figure S22. Size-dependent sensitivity is used to correct particle-phase intensity according to the size of the injected seeds listed in Table S1. This size-dependent sensitivity was determined from mixed SOA generated in CLOUD chamber from Lee et al. (2021).

175

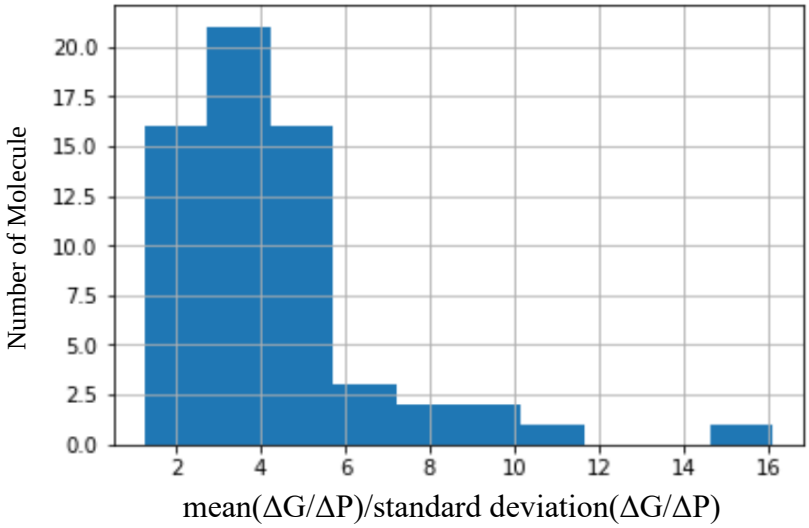

Figure S23. Histogram of mean(*ΔG/ΔP*)/standard deviation(*ΔG/ΔP*) from computation the *ΔG/ΔP* of 62 molecules with 5 data points (condensation sinks) for each species (Table S4).

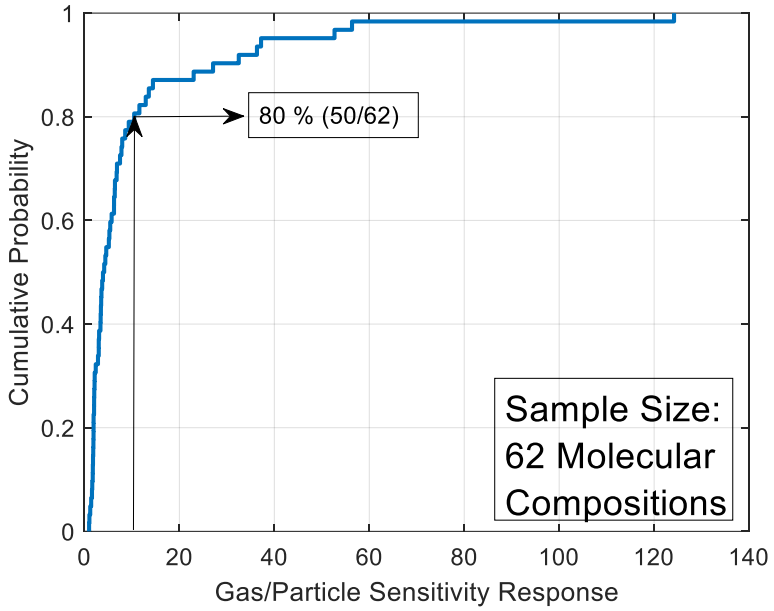

Figure S24. Cumulative distribution of *ΔG/ΔP* sensitivity response, 80% of the molecules have higher gas-phase sensitivity responses up to 11 in comparison to particle-phase.

This means that up to 80% gas phase measurement is up to 11 times more sensitive than what is measured in particle phase as anticipated from size-dependent sensitivity shown in Figure S22. As a result, the gas-phase intensity requires correction so that the sensitivity between gas phase and particle phase is equal to 1.

In an ideal situation, if the sensitivity of *ΔG* is equal to the sensitivity of *ΔP*, then there will be no correction needed. However, a correction is needed for gas-phase intensity described as follows. To understand the change of *ΔG/ΔP* sensitivity response, the *ΔG/ΔP* sensitivity response was logarithmically transformed for parameterization using molecular information as shown in Figure S25.

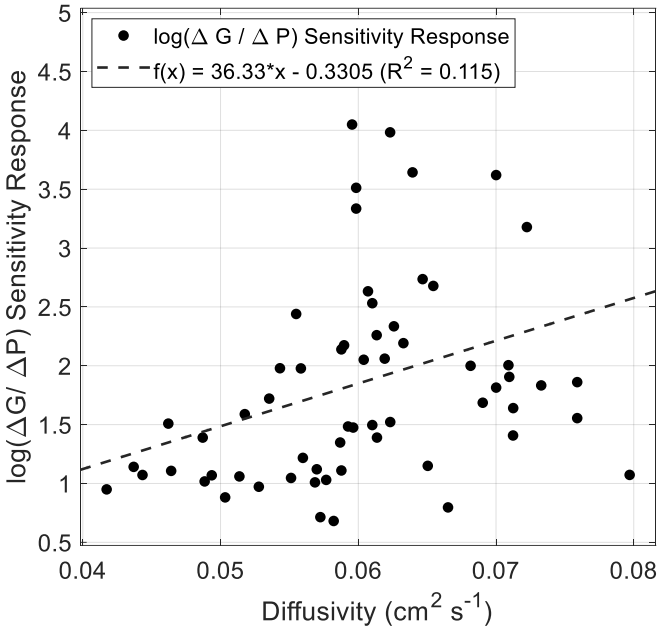

Figure S25. *ΔG/ΔP* sensitivity response of the Dual-EESI. The sensitivity response was logarithmically transformed as the function of diffusivity in air. The molecular information (number of carbon, hydrogen, and oxygen) are used for estimating binary gas diffusivity according to Fuller et al. (1966).

Table S4. Molecules included for calibration between gas/particle sensitivity of the Dual-EESI shown in Figures S22-S25 using condensation sink experiment under constant oxidized gas production rate.

$C_5H_6O_3$	$C_9H_{12}O_{2\text{-}5,7}$	$C_{12}H_{18}O_5$
$C_5H_8O_4$	$C_9H_{13}O_{3\text{-}4}$	$C_{12}H_{20}O_6$
$C_6H8O_{3\text{-}4}$	$C_9H_{14}O_{3\text{-}6}$	$C_{13}H_{20}O_6$
$C_6H_{10}O_3$	$C_9H_{15}O_{4,6}$	$C_{13}H_{24}O_4$
$C_6H_{12}O_3$	$C_9H_{16}O_{4\text{-}5}$	$C_{15}H_{18}O_2$
$C_7H_8O_{2\text{-}3}$	$C_{10}H_{14}O_{5\text{-}7}$	$C_{15}H_{20}O_6$
$C_7H_{10}O_{2\text{-}5,8}$	$C_{10}H_{16}O_5$	$C_{15}H_{22}O_5$
$C_8H_{10}O_{2\text{-}4}$	$C_{10}H_{22}O_3$	$C_{16}H_{22}O_7$
$C_8H_{12}O_{2\text{-}5}$	$C_{11}H_{16}O_{5\text{-}6}$	$C_{17}H_{22}O_6$
$C_8H_{14}O_{4,6}$	$C_{12}H_{16}O_5$	$C_{18}H_{24}O_8$
$C_9H_8O_3$		

References

MicroFab Technologies Inc., [online] Available from: http://www.microfab.com/other-systems2/vaporjet (Accessed 15 February 2021).

SilcoTek GmbH, [online] Available from: https://www.silcotek.com/silcod-technologies/silconert-inert-coating (Accessed 15 February 2021).

Donahue, N. M., Epstein, S. A., Pandis, S. N. and Robinson, A. L.: A two-dimensional volatility basis set: 1. organic-aerosol mixing thermodynamics, Atmos. Chem. Phys., 11(7), 3303–3318, doi:10.5194/acp-11-3303-2011, 2011.

Fuller, E. N., Schettler, P. D. and Giddings, J. C.: A new method for prediction of binary gas-phase diffusion coefficients, Ind. Eng. Chem., 58(5), 18–27, doi:10.1021/ie50677a007, 1966.

Gormley, P. G. and Kennedy, M.: Diffusion from a Stream Flowing through a Cylindrical Tube, Proc. R. Irish Acad. Sect. A Math. Phys. Sci., 52, 163–169 [online] Available from: http://www.jstor.org/stable/20488498 (Accessed 21 February 2021), 1949.

Krechmer, J. E., Day, D. A., Ziemann, P. J. and Jimenez, J. L.: Direct Measurements of Gas/Particle Partitioning and Mass Accommodation Coefficients in Environmental Chambers, Environ. Sci. Technol., 51(20), 11867–11875, doi:10.1021/acs.est.7b02144, 2017.

Kulmala, M. and Wagner, P. E.: Mass accommodation and uptake coefficients - A quantitative comparison, J. Aerosol Sci., 32(7), 833–841, doi:10.1016/S0021-8502(00)00116-6, 2001.

Lee, C. P., Surdu, M., Bell, D. M., Lamkaddam, H., Wang, M., Ataei, F., Hofbauer, V., Lopez, B., Donahue, N. M., Dommen, J., Prevot, A. S. H., Slowik, J. G., Wang, D., Baltensperger, U. and El Haddad, I.: Effects of aerosol size and coating thickness on the molecular detection using extractive electrospray ionization, Atmos. Meas. Tech., 14(9), 5913–5923, doi:10.5194/amt-14-5913-2021, 2021.

Zhang, D. and Zhang, R.: Ozonolysis of α -pinene and B -pinene: Kinetics and mechanism, J. Chem. Phys., 122(11), 214305, doi:10.1063/1.1862616, 2005.